Nano Research

ISSN 1998-0124 CN 11-5974/O4
https://doi.org/10.26599/NR.2026.94908559

Research Article

# $CO_2$-philic NiNC nanocatalyst regulation mediated by imidazole-based ZIF for high-efficiency $CO_2$ electroreduction

Xin Cui[1,2], Xiaona Meng[1,2], Weixiong Huang[1,2], Bo Zhang[1,2], Ping Chen[1,2], Min Ruan[3](✉), Lilin Lu[1,2](✉)

[1] The State Key Laboratory of Refractories and Metallurgy, Wuhan University of Science and Technology, Wuhan 430081, China

[2] Hubei Province Key Laboratory of Coal Conversion and New Carbon Materials, Wuhan University of Science and Technology, Wuhan 430081, China

[3] Hubei Key Laboratory of Mine Environmental Pollution Control & Remediation, Mineral Processing Research Institute, Hubei Polytechnic University, Huangshi 435003, China

*Nano Res.*, **Just Accepted Manuscript** • https://doi.org/10.26599/NR.2026.94908559
**https://www.sciopen.com/journal/1998-0124** on Feb. 15, 2026

**TABLE OF CONTENTS (TOC)**

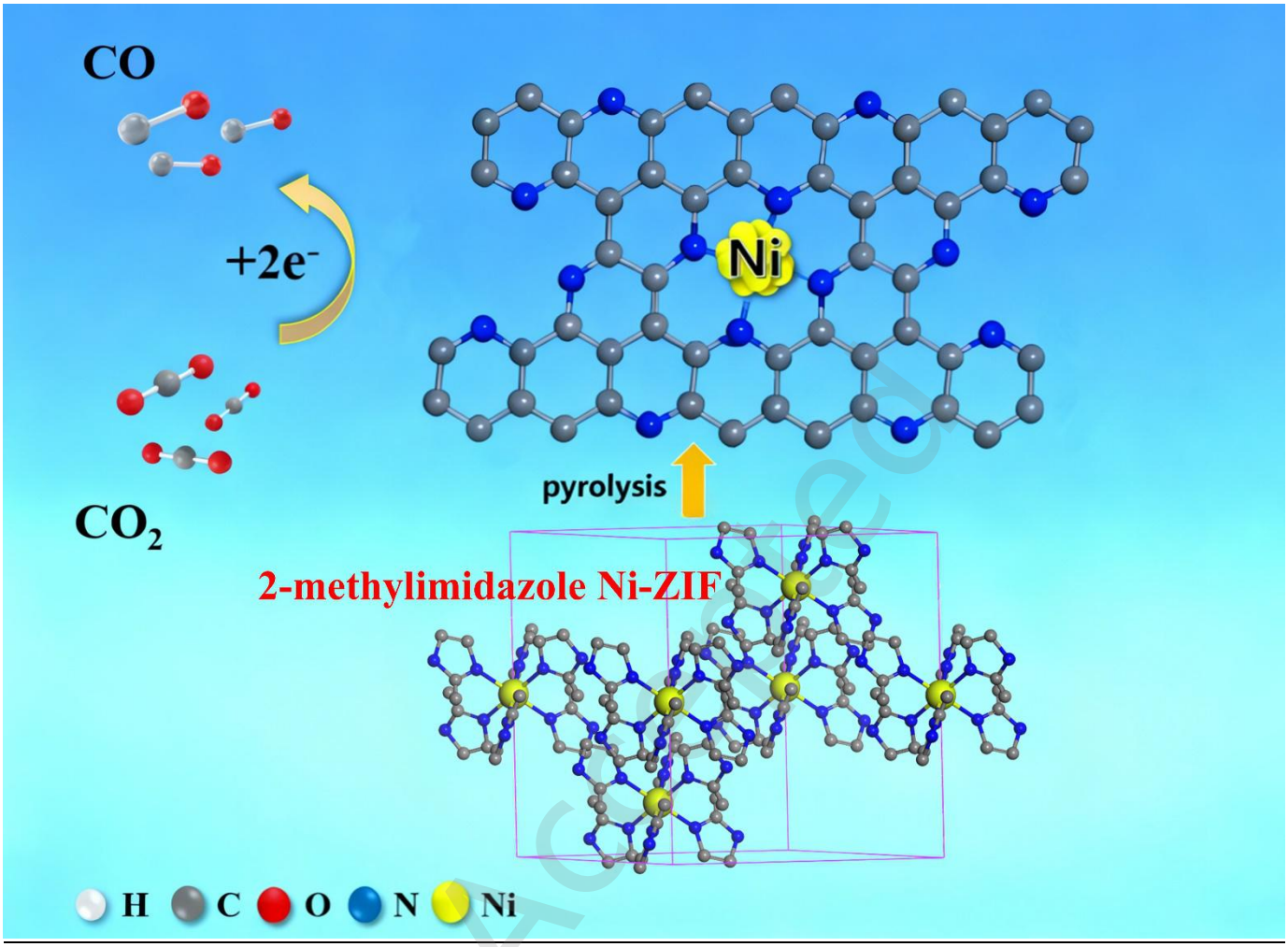


A highly efficient NiNC catalyst for $CO_2$RR is obtained by manipulating the nitrogen-containing species via imidazole-based ZIF precursor-mediated regulation strategy. Pyrolysis of 2-methylimidazole-based Ni-ZIF yields a Ni-N-C catalyst that efficiently drives the electrochemical reduction of $CO_2$ to CO.

Nano Research

Open Access

Research Article

# $CO_2$-philic NiNC nanocatalyst regulation mediated by imidazole-based ZIF for high-efficiency $CO_2$ electroreduction

Xin Cui,[1,2] Xiaona Meng,[1,2] Weixiong Huang,[1,2] Bo Zhang,[1,2] Ping Chen,[1,2] Min Ruan, [3] ✉, and Lilin Lu [1,2] ✉

[1] *The State Key Laboratory of Refractories and Metallurgy, Wuhan University of Science and Technology, Wuhan 430081, China*
[2] *Hubei Province Key Laboratory of Coal Conversion and New Carbon Materials, Wuhan University of Science and Technology, Wuhan 430081, China*
[3] *Hubei Key Laboratory of Mine Environmental Pollution Control & Remediation, Mineral Processing Research Institute, Hubei Polytechnic University, Huangshi 435003, China*

**Received:** 2 December 2025; **Revised:** 22 January 2026; **Accepted:** 11 February 2026

✉Address correspondence to Lilin Lu, lulilin@wust.edu.cn; Min Ruan, ruanmin@hbpu.edu.cn

**Cite this article:** *Nano Research*, **2026**, *19*, 94908559. https://doi.org/10.26599/NR.2026.94908559

**ABSTRACT:** Developing highly efficient catalyst for carbon dioxide reduction ($CO_2RR$) to convert $CO_2$ into carbon-based chemicals and reduce anthropogenic carbon emission is desirable but challenging. In this work, a high-activity NiNC-2mIM catalyst has been developed via pyrolysis of 2-methylimidazole Ni-ZIF precursor, it exhibits excellent performance for $CO_2$ reduction producing CO, with Faradaic efficiency ($FE_{CO}$) of about 98% and a current density of 55 mA $cm^{-2}$ at -1.0 V (vs. RHE), outperforming the investigated NiNC-IM and NiNC-2eIM (derived from imidazole Ni ZIF precursor and 2-ethylimidazole Ni ZIF precursor, respectively) in this work and many previously reported Ni-based nanocatalysts. Mechanism studies demonstrate that 2-methylimidazole ligand induces higher content of pyridinic N species in the NiNC-2mIM catalyst, which enhances the affinity for $CO_2$ and provides low-polarity and high-activity Ni-N motif for $CO_2RR$. This work develops a novel imidazole-based ZIF mediated regulation strategy for engineering pyridinic-N-rich N-doped carbon supported Ni nanocatalyst to highly efficiently catalyze $CO_2$ reduction producing CO.

**KEYWORDS:** electrochemical $CO_2$ reduction, NiNC nanocatalyst, imidazole-based Ni ZIF precursor, improved affinity for $CO_2$, high-activity pyridinic N-Ni sites.



## 1 Introduction

Electrochemical carbon dioxide reduction to value-added products provides a sustainable route to mitigate the challenge of elevated atmospheric $CO_2$ concentrations and the storage of intermittent renewable energy[1]-[3] Among various electrochemical carbon dioxide reduction reaction ($CO_2RR$) pathways, the two-electron reduction of $CO_2$ to carbon monoxide (CO) or formate (HCOOH) is a promising one due to its relatively low thermodynamic potential and rapid kinetics [4], [5]. The broad applicability of CO as a syngas component and precursor for Fischer-Tropsch synthesis and other industrial processes make the conversion of $CO_2$ to CO especially attractive over other conversion pathways [6]-[8]. The key to achieving high CO selectivity in $CO_2RR$ is developing high-efficiency catalyst that possesses low $CO_2RR$ overpotential and long-term durability [9]-[11] and getting deep insight into the catalytic mechanism [12], [13]. In addition, promotion the electrochemical current density to realize industry-level $CO_2RR$ with high CO selectivity is desirable but remains a pressing challenge due to the sluggish $CO_2$ activation kinetics as compared to competitive hydrogen evolution reaction (HER) [14], [15].

Transition metal-nitrogen-carbon (M-NC) has emerged as the most promising catalyst for electrocatalytic $CO_2$ reduction [16], [17]. Among them, nickel-based catalysts (Ni-N-C) are particularly interesting because of the low cost, environmental benignity, and intrinsic catalytic activity of nickel for CO production[18]-[21]. The electrocatalytic performance of Ni-NC strongly depends on the local coordination environment of Ni sites, especially the Ni-$N_x$ moieties, which serve as the primary active centers for $CO_2$ adsorption and reduction [22], [23]. Enhancing the affinity of the catalyst surface for $CO_2$ is an important pathway of improving $CO_2RR$ activity of Ni-NC catalyst. Some strategies including interfacial microenvironment regulation and introducing basic nitrogen functionalities have been developed to promote $CO_2$ adsorption on active site and diffusion in catalyst material[24]-[26].

Due to high content of nitrogen and excellent metal-chelating ability of imidazole ligands, zeolite-imidazolate-frameworks (ZIFs) have been extensively used to construct Ni-NC catalysts via high-temperature pyrolysis[27], [28]. Imidazolium-based materials and their derivatives have emerged as promising candidates for $CO_2RR$, the N-heterocyclic carbenes (NHCs) functionalized metal–organic framework (UiO-66-NHC-CO2) efficiently catalyzed $CO_2RR$ for CO production [29], [30].

Upon high-temperature pyrolysis, ZIFs provides the desirable Ni-NC motif for catalytic $CO_2RR$ on one hand, and serves as carbon and nitrogen sources to produce conductive N-doped carbon, which is favorable for charge transfer, active site stabilization, and $CO_2$ adsorption[31]-[34]. Additionally, imidazole-derived nitrogen species can effectively regulate the

electron density on transition metal center, thus improving the $CO_2$-adsorption and activation capability to highly efficiently catalyze $CO_2$RR [35].

Despite the excellent performance of organic nitrogen-derived Ni-N catalysts for highly selectively CO production from $CO_2$RR, the low reduction current density is needed to be improved to promote the efficiency of electrocatalytic $CO_2$ conversion [36]. Introducing electron-withdrawing or donating groups into organic nitrogen ligand can effectively tailor the activity of Ni-NC catalyst [37]. In this work, a novel imidazole precursor-mediated regulation strategy has been developed to manipulate the Ni-N active sites and the $CO_2$ affinity of NiNC nanocatalyst surface. The as-prepared NiNC-2mIM catalyst, obtained from pyrolysis of 2-methylimidazole Ni-ZIF, possesses abundant pyridinic-N-Ni sites and relatively high affinity for $CO_2$ gas bubble, therefore exhibiting excellent activity and selectivity for CO production from $CO_2$RR. The catalytic mechanism has been explored by combination of experimental investigations and density function theory (DFT) calculations. The Ni-ZIF precursors containing 2-methylimidazole ligand induced the formation of higher content of pyridinic-N species during pyrolysis process than those containing imidazole ligand or 2-ethylimidazole ligand, forming Ni-N sites with lower polarity and $CO_2$-philic surface of the NiNC-2mIM catalyst, therefore providing higher catalytic activity and selectivity for electroreduction $CO_2$ to CO.

## 2 Experimental details

### 2.1 Materials

Imidazole ($C_3H_4N_2$), 2-methylimidazole ($C_4H_6N_2$), 2-ethylimidazole ($C_5H_8N_2$) were purchased from Shanghai Aladdin Biochemical Technology Co., Ltd., nickel nitrate hexahydrate ($Ni(NO_3)_2{\cdot}6H_2O$) was purchased from Sinopharm Chemical Reagent Co., Ltd., and Nafion D-521 dispersion (5% w/w in water/ethanol mixture) was obtained from Alfa Aesar company. All the chemicals were used directly without further purification, and deionized water was used in all experiments.

### 2.2 Catalysts preparation

Ni-nanoparticle catalysts were synthesized by pyrolyzing the Ni-ZIF (zeolitic imidazolate framework) precursors including Ni-IM, Ni-2mIM and Ni-2eIM, which are obtained from reaction between nickel ion and imidazole ligands (including imidazole, 2-methylimidazole and 2-ethylimidazole) at room temperature, and denoted as NiNC-IM, NiNC-2mIM and NiNC-2eIM, respectively. Taking NiNC-2mIM as an example, the typical synthesis procedure is as follows: 4.51 g of $Ni(NO_3)_2{\cdot}6H_2O$ and 6.36 g of 2-methylimidazole were dissolved in 80 mL of deionized water, and stirred at room temperature for 12 h. Subsequently, the precipitate was recovered by filtration, and washed with water and ethanol for three times, then dried in an oven at 60°C to obtain the Ni-2mIM ZIF precursor. Finally, the precursor was transferred into a tube furnace and heated to 800 °C with a ramping rate of 5°C/min in nitrogen atmosphere, and kept at 800°C for 2 h to obtain the NiNC-2mIM catalyst. Similar procedure is used to prepare the NiNC-IM and NiNC-2eIM catalysts.

### 2.3. Electrochemical measurements

The $CO_2$RR performances of the investigated catalysts were tested using a three-electrode system on an electrochemical workstation (CHI660E, CH Instrument, Inc) in a typical H-type cell. The cathode chamber and the anode chamber, separated by an ion exchange membrane (Nafion-117), were both injected with 30 ml 0.5M $KHCO_3$ (pH=7.2 after $CO_2$ saturation) electrolyte solution. The catalyst ink was prepared by dispersing 6.0 mg of catalyst into 1.0 mL of water/ethanol solution (1:1 v/v) together with 50.0 μL (5.0 wt%) Nafion, and then coated evenly onto carbon paper to obtain the working electrode with catalyst loading of 1.0 mg cm $^{-2}$. Platinum mesh and an Ag/AgCl (3.0 M KCl) electrode were utilized as the counter and reference electrodes, respectively. All potentials were referenced to the reversible hydrogen electrode (RHE) using the following equation:

E (*vs*. RHE) = E (*vs*. Ag/AgCl) + 0.197 V + 0.0591 × pH (V)

Linear sweep voltammetry (LSV) curve was recorded in $CO_2$-saturated 0.5 M $KHCO_3$ electrolyte, with a sweep rate of 5 mV $s^{-1}$ in the potential range from 0 to -1.2 V (vs. RHE). $CO_2$ was continuously bubbled into the cathodic electrolyte (20 sccm) under magnetic stirring during $CO_2$RR tests. Gas-phase products were quantified using an online gas chromatograph (GC, FuLi 9790 Ⅱ) equipped with a thermal conductivity detector (TCD) and a flame ionization detector (FID). The Faradaic efficiency (*FE*) of the product was calculated according to the following equation:

$$FE=\frac{n\,z\,F}{Q}\times 100\%$$

where n is the number of moles of a product, z is the number of transformed electrons for targeted product (for CO or $H_2$, z = 2), F is the Faraday constant (96485 C $mol^{-1}$), Q is the total charge during the reduction reaction.

Tafel slope was derived from the Tafel equation $\eta$ = a + b*log $j$, where $\eta$ was overpotential, $j$ was current density, and b is the Tafel slope. Cyclic voltammetry (CV) curves were recorded at different sweep rates over the non-Faraday potential range to measure electrochemical double layer capacitance ($C_{dl}$). Electrochemical impedance spectrum (EIS) was collected in the frequency range of $10^5$ to $10^{-2}$ Hz, with an AC amplitude of 5 mV at a potential of -1.0 V (vs. RHE). Chronoamperometry was measured at -1.0 V (vs. RHE) to investigate catalytic durability.

### 2.4 Density functional theory (DFT) calculations

Density functional theory (DFT) calculations were carried out using the CASTEP code [39] based on a plane-wave pseudopotential. The exchange-correlation energy was treated within the generalized gradient approximation (GGA-PBE) [40], with ultrasoft pseudopotentials (USP) [41] and a 480 eV plane-wave cutoff. Geometry optimizations were conducted by using BFGS algorithm [42] without symmetry constraints, with convergence criteria set to $5\times10^{-6}$ eV/atom for energy, 0.01 eV/Å for forces and $5\times10^{-4}$ Å for displacements, respectively. Γ-centered 1×1×1 Monkhorst-Pack k-point grid was used for Brillouin zone sampling and SCF convergence was set as $1\times10^{-5}$ eV/atom. Reaction transition states were identified by linear synchronous transit (LST) and quadratic synchronous transit (QST) approaches [43] . The $CO_2$ adsorption free energy ($\Delta G_{ad}$) on N-Ni site was calculated as $\Delta G_{ad} = G_{cat} + G_{co2} - G_{cat+\,co2}$, where $G_{cat+\,co2}$, $G_{cat}$ and $G_{co2}$ were the calculated free energies of species adsorbed on N-Ni site, the bare N-Ni site, and the gas-phase $CO_2$ molecule, respectively.

## 3 Results and Discussion

### 3.1 Characterization of NiNC-IM, NiNC-2mIM and NiNC-2eIM catalysts

X-ray diffraction (XRD) patterns were recorded to characterize the phase composition of Ni-ZIF precursors and the prepared NiNC catalysts, respectively. The highly intensive diffraction peaks indicate that the imidazole-based Ni-ZIF precursors are successfully synthesized through coordination reaction between $Ni(NO_3)_2$ and imidazole ligands at room temperature (Figure 1a and S1) [44]. From the simulated XRD patterns which well match the experimental results, the simulated geometries of Ni-IM, Ni-2mIM and Ni-2eIM ZIFs are determined (Figure S2), demonstrating that different side chain in imidazole ligand induces substantially different geometries of Ni-ZIF precursors. After being pyrolyzed at 800 °C, Ni-ZIFs transformed into N-doped carbon supported Ni nanocatalyst, indicated by the XRD patterns of NiNC-IM, NiNC-2mIM and NiNC-2eIM catalysts. The diffraction peaks at 44.5°, 51.8°, and 76.4°, corresponding to metallic Ni (PDF#04-0850), confirm the formation of metallic Ni in NiNC-IM, NiNC-2mIM, and NiNC-2eIM catalysts (Figure 1b). A broad diffraction peak centered at approximately 26.2° can be ascribed to N-doped carbon, confirming the formation of the N-doped carbon derived from the imidazole ligands (Figure S3). Scanning electron microscopy (SEM) images show that the Ni-IM ZIF has the regular polyhedral morphology with relatively large size, whereas the Ni-2mIM and Ni-2eIM ZIFs have the irregular morphology (Figure 1c). From the SEM images of NiNC-IM, NiNC-2mIM and NiNC-2eIM catalysts, it can be observed that Ni nanoparticles are supported on N-doped carbon that is produced via high-temperature pyrolysis (Figure 1d). High-resolution TEM (HRTEM) images (Figure 1e) demonstrate that the Ni nanoparticles are encapsulated by graphitic N-doped carbon layers. The lattice fringes with an interplanar distance of 0.20 nm and 0.35 nm correspond to the (111) plane of the metallic Ni and the (002) plane of N-doped carbon, respectively. In addition, the ligand-dependent thickness of N-doped carbon layer is observed, the NiNC-2mIM possesses the thinnest N-doped carbon layer (approximately 2.66 nm), distinctly thinner than that of the NiNC-2eIM (~3.23 nm) and NiNC-IM (~5.74 nm). Ni particle-size analysis (Figure S4) reveals the diameters of Ni nanoparticles are approximately

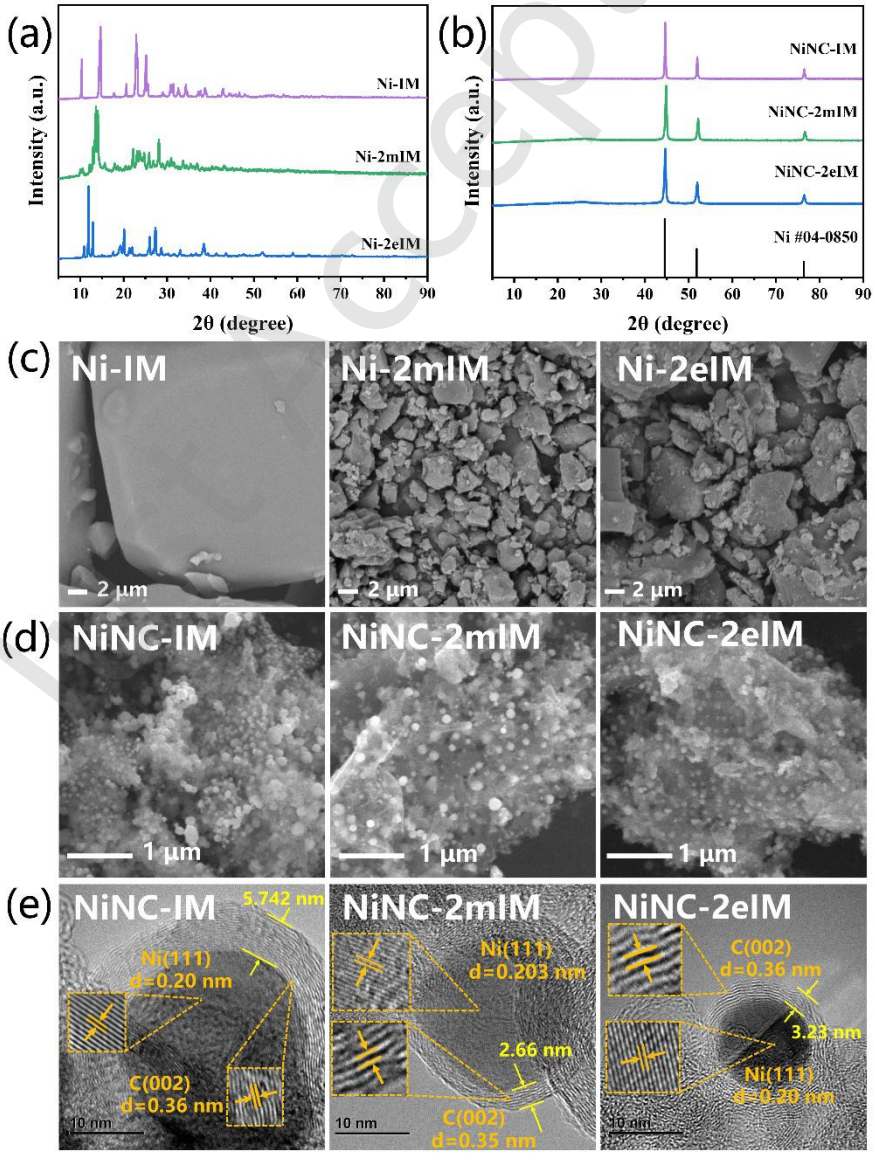


**Figure 1**(a) XRD patterns of Ni-IM, Ni-2mIM and Ni-2eIM ZIF precursors. (b) XRD patterns of NiNC-IM, NiNC-2mIM and NiNC-2eIM catalysts. (c) SEM images of Ni-IM, Ni-2mIM and Ni-2eIM ZIF precursors. (d) SEM images of NiNC-IM, NiNC-2mIM and NiNC-2eIM catalysts. (e) HRTEM images of NiNC-IM, NiNC-2mIM and NiNC-2eIM catalysts.

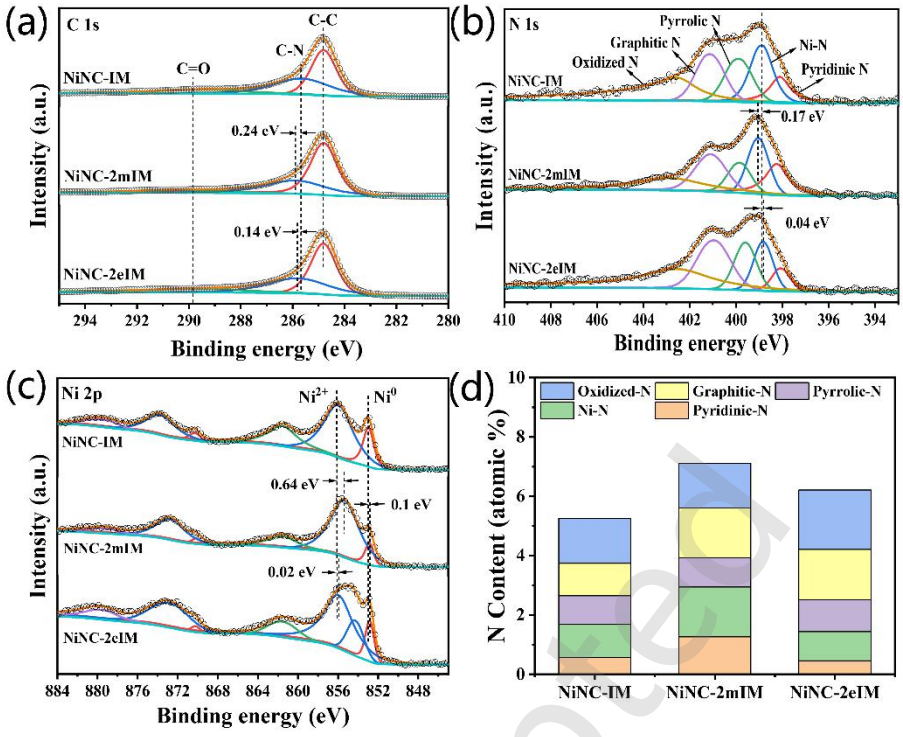


**Figure 2** (a) C 1s XPS spectra of NiNC-IM, NiNC-2mIM, and NiNC-2eIM, and (b) N 1s XPS spectra of NiNC-IM, NiNC-2mIM, and NiNC-2eIM. (c) Ni 2p XPS spectra of NiNC-IM, NiNC-2mIM, and NiNC-2eIM. (d) absolute N contents in NiNC-IM, NiNC-2mIM and NiNC-2eIM.

130.8 nm in NiNC-IM, 142.5 nm in NiNC-2mIM and 107.8 nm in NiNC-2eIM, respectively.

The electronic states of surface elements are investigated by X-ray photoelectron spectroscopy (XPS). The overall survey spectra confirm the existences Ni, O, N, and C elements in three investigated NiNC catalysts (Figure S5), the total N contents for NiNC-IM, NiNC-2mIM, and NiNC-2eIM are determined to be 5.26 at%, 7.11 at%, and 6.21 at%, respectively. In the high-resolution C 1s spectra (Figure 2a) of three investigated catalysts, the characteristic peaks for C-C, C-N, and C=O are observed. Among them, the binding energies of C-C and C=O are almost same for all catalysts, but the binding energy in C-N in the NiNC-2mIM is slightly higher than that in the NiNC-2eIM, and distinctly higher than that in the NiNC-IM, indicative of the higher oxidation state of C in the NiNC-2mIM as compared to NiNC-2eIM and NiNC-IM. In the high-resolution N 1s spectra, the peaks at 398.2, 398.9, 399.8, 401.2 and 404.2 eV can be attributed to pyridinic-N, N-Ni, pyrrolic-N, graphitic-N and oxidized-N, respectively [45] (Figure 2b). The N-Ni binding energy in the NiNC-2mIM undergoes a positive shift of about 0.17 eV, whereas that in the NiNC-2eIM undergoes a negative shift of about 0.04 eV, as compared to that in the NiNC-IM, indicating that the oxidation state of N in N-Ni in the NiNC-2mIM is distinctly higher those in the NiNC-IM and NiNC-2eIM. In the Ni 2p spectra, the peaks corresponding to $Ni^{2+}$ and $Ni^{0}$ species are observed for all investigated catalysts, confirming the coexistence of divalent nickel and metallic nickel in them (Figure 2c). However, the binding energy of $Ni^{2+}$ in the NiNC-2mIM is substantially lower than that in the NiNC-IM and NiNC-2eIM, signifying the higher electron density around $Ni^{2+}$ in the NiNC-2mIM than the cases in the other two catalysts. These results reveal that there is more remarkable electron donation from CN to $Ni^{2+}$, inducing higher oxidation state of C and N but lower oxidation state of $Ni^{2+}$ and resulting in a low degree of polarization of Ni-N bond in the NiNC-2mIM than in other two catalysts. The elemental composition (Figure 2d) from N 1s XPS spectra reveals that the contents of pyridinic-N and Ni-N are higher but the contents of pyrrolic-N, graphitic-N and oxidized-N in NiNC-2mIM are lower than the counterparts in the NiNC-IM and NiNC-2eIM catalysts, indicating that the 2-methylimidazole ligand is conducive to the formation of pyridinic-N species during pyrolysis of Ni-ZIF precursors. By combining the total N contents with the relative proportions of different N species, the absolute content of pyridinic N in in NiNC-2mIM is determined to be about 1.26 at%, distinctly higher than those of NiNC-IM (0.57 at%) and NiNC-2eIM (0.46 at%), revealing that the NiNC-2mIM catalyst possesses the highest content of pyridinic-N species. The stronger basicity of

pyridinic-N than pyrrolic-N and graphitic-N endows pyridinic-N with higher degree of electron density donation to $Ni^{2+}$, resulting in the Ni-N motifs with lower polarity in the NiNC-2mIM catalyst than in the other catalysts.

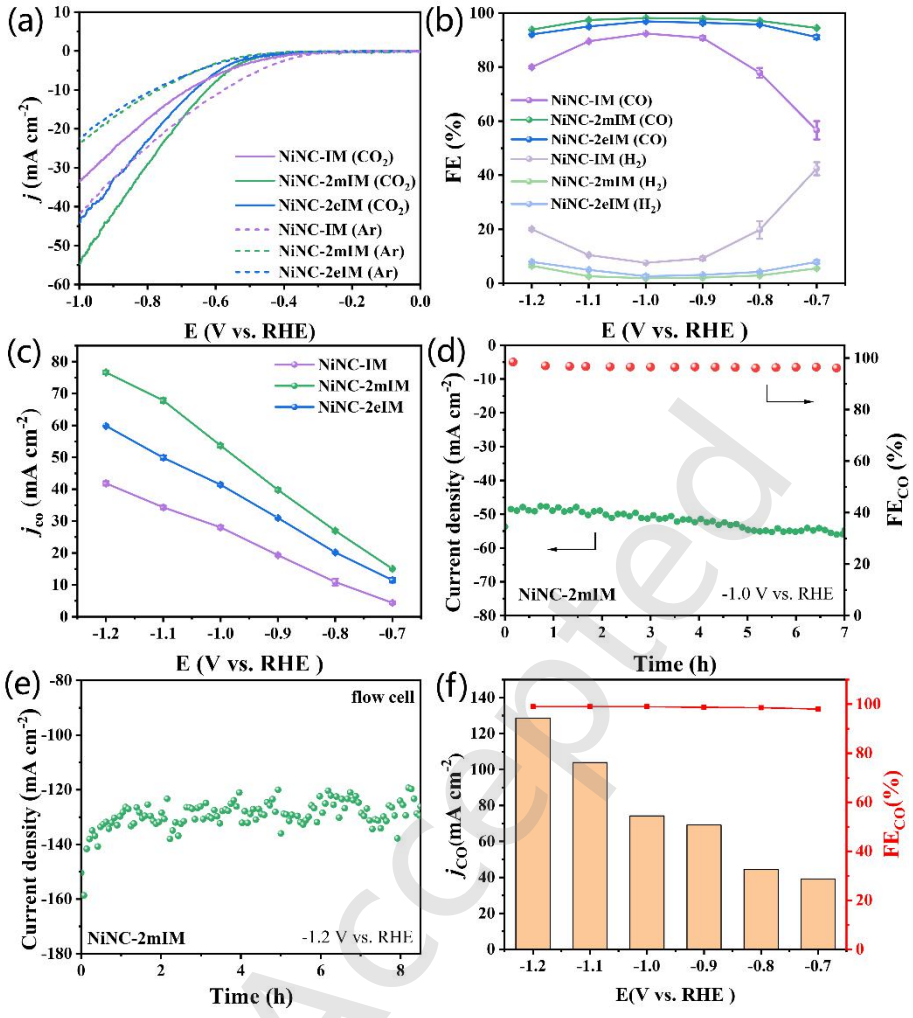


**Figure 3** (a) Linear sweep voltammetry curves obtained in Ar- and $CO_2$-saturated electrolyte (0.5 M $KHCO_3$ solution). (b) $FE_{CO}$ and $FE_{H2}$ of NiNC-IM, NiNC-2mIM and NiNC-2eIM at -0.7~-1.2 V (vs. RHE). (c) $j_{CO}$ of NiNC-IM, NiNC-2mIM and NiNC-2eIM at -0.7~-1.2 V (vs. RHE). (d) Durability testing of NiNC-2mIM at -1.0 V (vs. RHE) in the H-type cell. (e) Durability testing of NiNC-2mIM at -1.2 V (vs. RHE) in the flow cell. (f) $j_{CO}$ and $FE_{CO}$ of NiNC-IM, NiNC-2mIM and NiNC-2eIM at -0.7~-1.2 V (vs. RHE).

### 3.2 Electrochemical CO2RR performances of NiNC-IM, NiNC-2mIM and NiNC-2eIM catalysts

The $CO_2$RR performances of the investigated NiNC-IM, NiNC-2mIM and NiNC-2eIM were evaluated in an H-type cell. Linear sweep voltammetry (LSV) curves (Figure 3a) recorded respectively in Ar- and $CO_2$-saturated electrolyte show that the current density in $CO_2$-saturated electrolyte is substantially higher than that in Ar-saturated electrolyte for the NiNC-2mIM and NiNC-2eIM, indicative of their remarkable catalytic activity for $CO_2$RR. However, for the NiNC-IM catalyst, the current density in $CO_2$-saturated electrolyte is distinctly lower than that in Ar-saturated electrolyte, this should be explained by its relatively low $CO_2$RR activity and the inhibition effect of $CO_2$ on hydrogen evolution reaction, thus reducing the current density of electrolysis reaction. Notably, NiNC-2mIM demonstrates a substantially higher current density in $CO_2$-saturated electrolyte compared to NiNC-IM and NiNC-2eIM, highlighting its superior electrochemical $CO_2$RR performance. Within the potential range of -0.7 to -1.2 V (vs. RHE), NiNC-2mIM exhibits higher Faradaic efficiency for CO ($FE_{CO}$) than NiNC-IM and NiNC-2eIM (Figure 3b), the $FE_{CO}$ of NiNC-2mIM reaches 98% at -1.0 V (vs. RHE), demonstrating its excellent CO selectivity. For all investigated catalysts, the $FE$ for $H_2$ production ($FE_{H2}$) is significantly lower than $FE_{CO}$ at all tested potentials. Notably, the $FE_{H2}$ of NiNC-IM is remarkably higher than those for NiNC-2mIM and NiNC-2eIM, indicating its higher activity for hydrogen evolution reaction, confirmed by the higher current density in Ar-saturated electrolyte than in $CO_2$-saturated electrolyte in LSV test. In addition, NiNC-2mIM achieves higher CO partial current density ($j_{CO}$) than NiNC-IM and NiNC-2eIM, and $j_{CO}$ increases linearly with reduction potential, reaching 78 mA $cm^{-2}$ at -1.2 V (vs. RHE), remarkably higher than those of NiNC-IM (42 mA $cm^{-2}$) and NiNC-2eIM (60 mA $cm^{-2}$), indicative of the highest catalytic efficiency of $CO_2$RR among the three investigated catalysts (Figure 3c). A long-term chronoamperometry test of the NiNC-2mIM at -1.0 V (vs. RHE) shows that the $FE_{CO}$ maintains above 90% with stable $j_{CO}$ (maintaining about 55 mA $cm^{-2}$) after seven-hour test, manifesting its excellent catalytic durability for $CO_2$RR (Figure 3d). The NiNC-2eIM exhibits a similar catalytic durability to NiNC-2mIM, however, the current density remarkably decreases when NiNC-IM undergoes a long-time electrochemical test

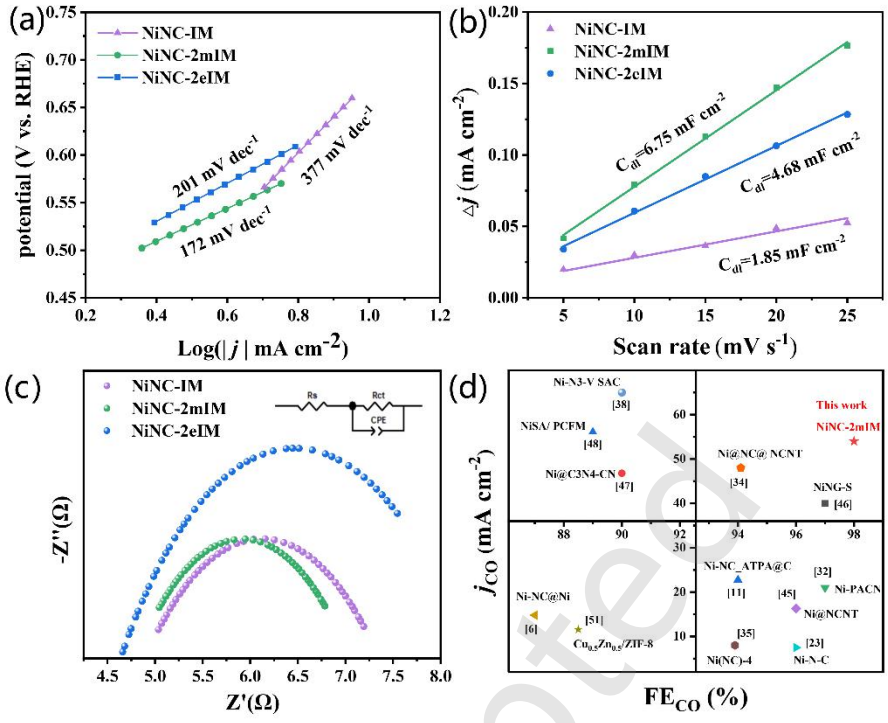


**Figure 4** (a) Tafel plots and (b) electrochemical $C_{dl}$ of the NiNC-IM, NiNC-2mIM and NiNC-2eIM catalysts. (c) EIS spectra of the NiNC-IM, NiNC-2mIM and NiNC-2eIM catalysts at potential of -1.0 V (vs. RHE). (d) Comparison of current densities and $FE_{CO}$ of NiNC-2mIM catalyst from this work with those of previously reported Ni-based catalysts (corresponding reference numbers are given in brackets).

(Figure S6). Over cathodic potential ranging from - 0.7 V to -1.2V (vs. RHE), the turnover frequency (TOF) of CO2RR producing CO catalyzed by the NiNC-2mIM is substantially higher than that catalyzed by the NiNC-2eIM and the NiNC-IM. At the cathodic potential of -1.2V (vs. RHE), TOF for the NiNC-2mIM is determined to be about 791.17 h-1, distinctly higher than the TOF (530.86 h-1) for the NiNC-2mIM and significantly higher than the TOF (159.61 h-1) for the NiNC-IM (Figure S7). These distinctly different performances of the investigated NiNC catalysts underscore the effect of imidazole ligand on the prepared NiNC configuration and the crucial role of the pyridinic N-Ni motif in enabling selective CO production from $CO_2$RR. To mitigate the effect of limited $CO_2$ diffusion in electrolyte, the catalytic performance of the NiNC-2mIM was evaluated in a flow cell with 0.5M $KHCO_3$. Over the tested cathodic potentials, the current density is substantially improved as compared to that in H-type cell. A current density of ~130 mA $cm^{-2}$ can be achieved at -1.2 V (vs. RHE), about two-fold higher than that in the H-type cell, while maintaining ~99% CO selectivity (Figure 3e and f).

Tafel slope analysis (Figure 4a) shows that NiNC-2mIM possesses a Tafel slope of about 172 mV $dec^{-1}$, significantly lower than those of NiNC-IM (377 mV $dec^{-1}$) and NiNC-2eIM (201 mV $dec^{-1}$), indicating the faster electrochemical $CO_2$RR kinetics on the NiNC-2mIM catalyst. Electrochemical double-layer capacitance ($C_{dl}$) was measured based on cyclic voltammetry (CV) at different sweep rates in the non-Faradaic region to estimate the electrochemical surface area (ECSA) (Figure S8). The $C_{dl}$ of NiNC-2mIM is determined to be about 6.75 mF $cm^{-2}$, considerably higher than those of NiNC-IM (1.85 mF $cm^{-2}$) and NiNC-2eIM (4.68 mF $cm^{-2}$) (Figure 4b), indicating that NiNC-2mIM possesses more electrochemically active sites on the surface. Electrochemical impedance spectroscopy (EIS) (Figure 4c) reveals that the NiNC-2mIM catalyst exhibits the smallest impedance arc radius among them, which indicates the lowest charge transfer resistance ($R_{ct}$) that favors the reduction kinetics of adsorbed $CO_2$. A comparison of the best-performance NiNC-2mIM in this work with previously reported catalysts manifests that it outperforms most of Ni-nanoparticle catalysts, exhibiting the outstanding catalytic performances for $CO_2$RR (Figure 4d). As shown above, the high $CO_2$RR kinetics, high ECSA and low charge-transfer resistance of the NiNC-2mIM contribute importantly to its excellent $CO_2$RR performance, the abundant pyridinic N-Ni active sites might be responsible for its superior intrinsic $CO_2$RR activity.

### 3.3. Mechanism studies of CO2RR catalyzed by the NiNC-IM, NiNC-2mIM and NiNC-2eIM catalysts

To get insight into the origin of the different CO2RR performances of NiNC-IM, NiNC-2mIM and NiNC-2eIM, their affinity for $CO_2$ was investigated by underwater $CO_2$ bubble contact angle measurement. As shown, NiNC-IM, NiNC-2mIM and NiNC-2eIM exhibit different affinities for $CO_2$ (Figure 5a). Underwater $CO_2$ bubble was unable to be stably adsorbed on the surfaces of the NiNC-IM, it moved rapidly off the surface within 0.04 seconds, indicating that the NiNC-IM catalyst has an aerophobic surface and exhibits low affinity for $CO_2$. For the NiNC-2mIM and NiNC-2eIM catalysts, underwater $CO_2$ bubble could stay on the surface stably, and then permeated rapidly into the NiNC-2mIM and NiNC-2eIM catalyst material. After being adsorbed on the surface for 0.02s, the contact angles on the NiNC-2mIM and NiNC-2eIM surface are 42° and 85°, respectively. After 0.04 s, the $CO_2$ bubble completely permeated into the NiNC-2mIM, whereas it stayed on the surface of the NiNC-2eIM with a contact angle of about 80°. These results

show that the NiNC-2mIM has more aerophilic nature and exhibits higher affinity for $CO_2$ than the NiNC-2eIM, the higher content of pyridinic N species derived from 2-methylimidozle ligand might be responsible for the enhanced $CO_2$ affinity of NiNC-2mIM.

partial current density also undergo a remarkable decrease (Figure 5d). In addition, $H_3PO_4$ treatment leads to a remarkable decrease in the ESCA, as indicated by the CV scans at different sweep rates (Figure S10a). The $C_{dl}$ decreases to 4.06 mF $cm^{-2}$, which is lower than the $C_{dl}$ of fresh NiNC-2mIM and that of the

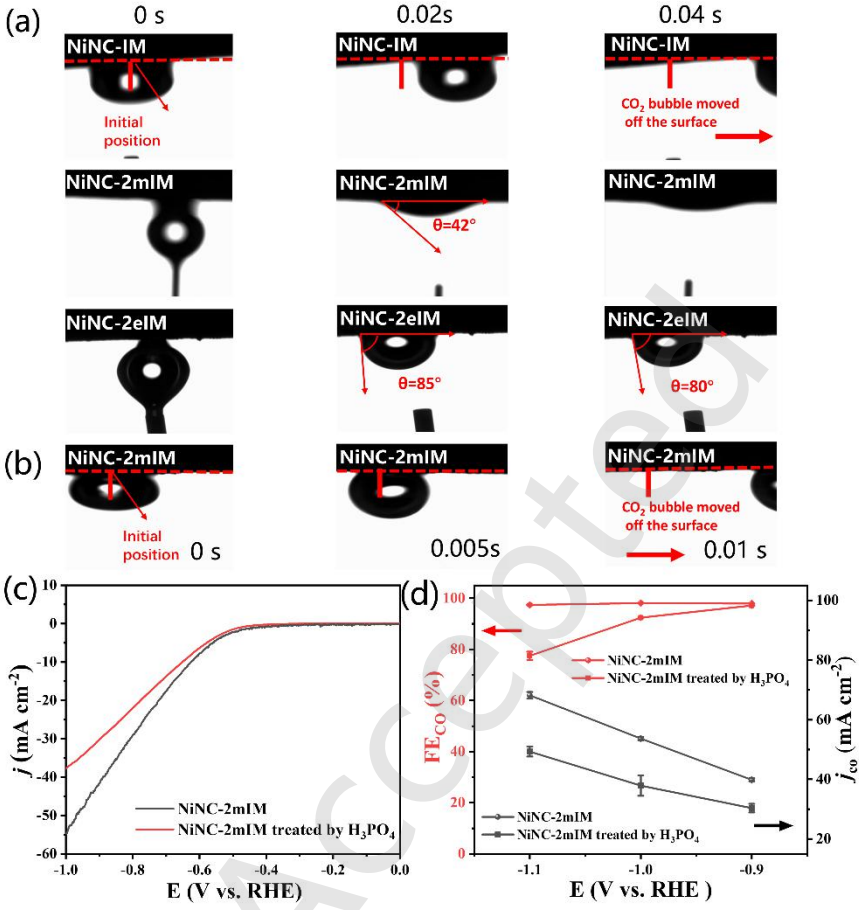


**Figure 5** The $CO_2$ bubble affinity measurements under water of (a) NiNC-IM, NiNC-2mIM, NiNC-2eIM and (b) NiNC-2mIM treatec by $H_3PO_4$. (c) LSV curves and (d) $FE_{CO}$ and $j_{CO}$ for the fresh NiNC-2mIM and the $H_3PO_4$ treated NiNC-2mIM.

To verify the key role of pyridinic-N-Ni sites at the interface between the Ni nanoparticle and the N-doped carbon in the $CO_2$RR, a Ni nanoparticle catalyst supported on carbon support (nitrogen-free Ni/C catalyst, Figure S9a) was prepared by pyrolysis of the mixture of nickel nitrate and glucose (as carbon source) at 800℃ in Ar atmosphere to catalyze $CO_2$RR . The results manifest that the Ni/C catalyst exhibits negligible activity for $CO_2$RR producing CO ($FE_{CO}$ <5%) but provides remarkably high activity for HER ($FE_{H2}$ > 95%), confirming that the Ni-N sites rather than Ni nanoparticle are the active sites for $CO_2$RR producing CO (Figure S9b). Furthermore, the NiNC-2mIM was treated by $H_3PO_4$ to block the pyridinic-N site to explore the effect of pyridinic-N on the $CO_2$RR performance [49],[50]. First, underwater $CO_2$ bubble contact angle measurement was performed, and the result shows that its affinity for $CO_2$ undergoes a dramatically decrease, the $CO_2$ bubble was unable to stay on the surface stably, characterized by rapid sliding and detachment within 0.01 s of interfacial contact (Figure 5b). This indicates the aerophilic surface of the NiNC-2mIM has been transformed into an aerophobic surface upon protonation of pyridinic N while being treated by $H_3PO_4$. LSV curves demonstrate that the $H_3PO_4$ treatment leads to a substantially decrease of current density (Figure 5c), and the $FE_{CO}$ and CO

NiNC-2eIM (Figure S10b). In the EIS plot, an increase in the diameter of impedance semicircle as compared to the fresh NiNC-2mIM is induced by $H_3PO_4$ treatment, indicating that the surface charge transfer resistance of the NiNC-2mIM has been substantially enhanced (Figure S10c). Tafel plot decreases from 189 mV $dec^{-1}$ to 172 mV $dec^{-1}$, showing that $H_3PO_4$ treatment slightly influences the $CO_2$RR electrochemical kinetics on the NiNC-2mIM catalyst (Figure S10d).

High-resolution Ni 2p and N 1s XPS spectra of $H_3PO_4$-treated NiNC-2mIM catalyst reveal that the binding energies of Ni 2p and N 1s both undergo positive shift (0.01 eV for Ni 2p and 0.1 eV for N 1s) as compared with the fresh NiNC-2mIM catalyst (Figure 6a and 6b), the protonation of pyridinic N result in higher oxidation state of N on one hand, and the induced electron-withdrawing effect weakens the electron donation from pyridinic N to $Ni^{2+}$ on the other hand, therefore decreasing the affinity for $CO_2$ and increasing the Ni-N bond polarity, consistent with the results of underwater $CO_2$ bubble contact angle measurement. These results manifest that the pyridinic-N species contributes importantly to the excellent $CO_2$RR performance of the NiNC-2mIM, not only improving the affinity for $CO_2$ but also engineering low-polarity pyridinic-N-Ni site with higher intrinsic electrochemical activity. In order to explore

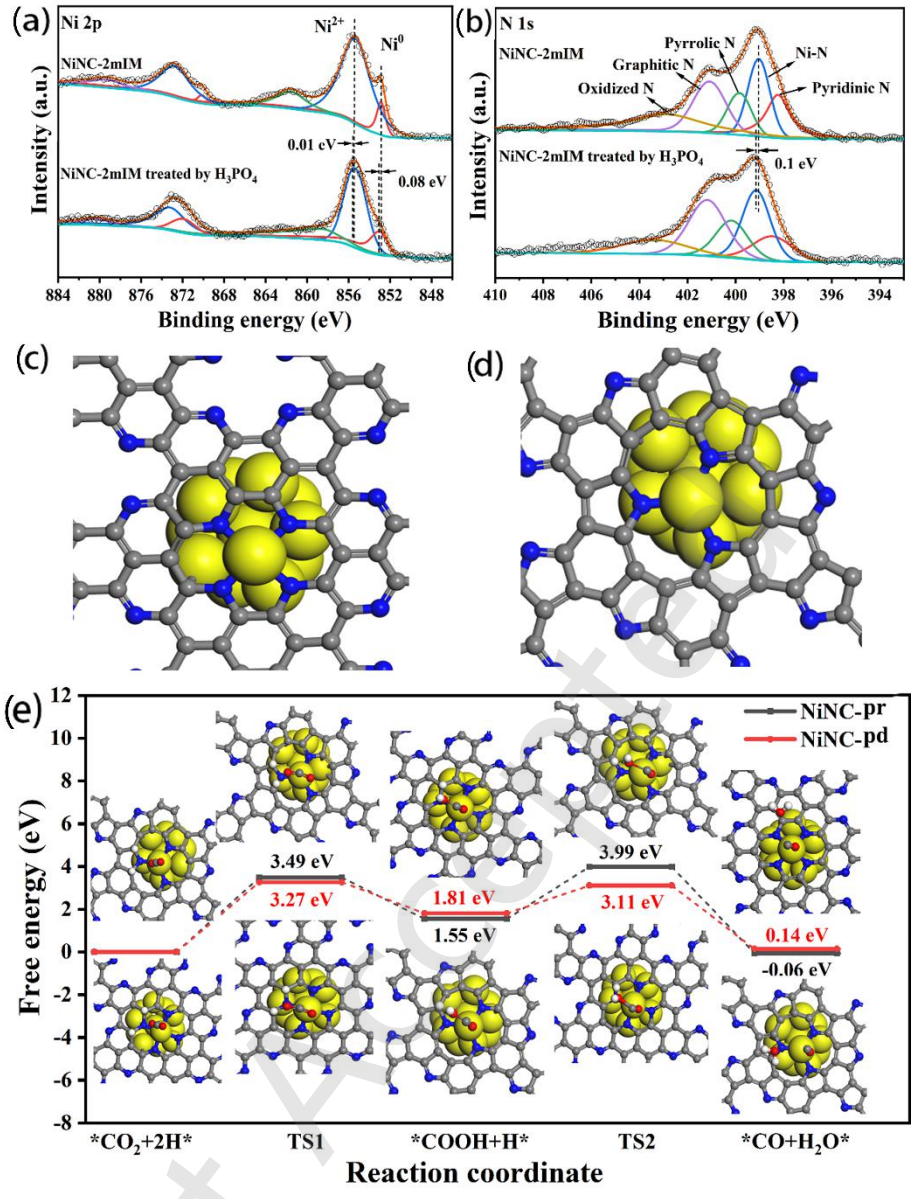


**Figure 6** High-resolution (a) Ni 2p and (b) N 1s XPS spectra of the fresh NiNC-2mIM and the $H_3PO_4$ treated NiNC-2mIM. The structural models of (c) pyridinic-N-Ni site (NiNC-pd) and (d) pyrollic-N-Ni site (NiNC-pr). (e) Energetic profiles of $CO_2$RR catalyzed by NiNC-pd and NiNC-pr.

the important role of pyridinic N-Ni site in catalytic $CO_2$RR activity, density functional theory (DFT) calculations are performed to comparatively study the $CO_2$ adsorption free energies and the energetic profiles of $CO_2$RR on pyridinic-N-Ni and pyrollic-N-Ni sites. The $Ni_{13}$ clusters with surface Ni atom coordination with pyridinic-N and pyrollic-N are used to simulate the two kinds of Ni-N sites in NiNC catalysts (denoted as NiNC-pd and NiNC-pr), respectively (Figure 6c and 6d). On the pyridinic-N-Ni site, the $CO_2$ adsorption free energy ($\Delta G_{ad}$) is calculated to be about 0.2 eV, signifying that the $CO_2$ molecule can be stably adsorbed on pyridinic-N-Ni site. However, on the pyrollic-N-Ni site, the calculated $\Delta G_{ad}$ is about -0.15 eV, indicating that $CO_2$ molecule can be stably adsorbed by pyrollic-N-Ni site. These results are in good agreement with the results of underwater $CO_2$ bubble contact angle measurement, the NiNC-2mIM catalyst which possesses the abundant pyridinic-N-Ni sites exhibits higher affinity for $CO_2$ than the other catalysts which have the relatively low content of pyridinic-N-Ni sites.

For the first reaction step, i.e., hydrogenation of $CO_2$ producing COOH intermediate, the energy barrier on NiNC-pd is calculated to be about 3.27 eV, distinctly lower than that on NiNC-pr by about 0.22 eV. For the second reaction step, i.e., COOH hydrogenation and dehydration producing CO, the calculated energy barrier on NiNC-pd is about 1.30 eV, substantially lower than that on NiNC-pr (2.44 eV). These results evidence that the pyridinic-N-Ni site exhibits remarkably higher activity for $CO_2$RR than pyrollic-N-Ni site, therefore, engineering abundant pyridinic-N-Ni sites on the catalyst surface would substantially improve the catalytic performance of NiNC catalyst for CO production from $CO_2$RR (Figure 6e). In this work, higher content of pyridinic N species and more abundant pyridinic-N-Ni sites in NiNC-2mIM catalyst than other catalysts endow NiNC-2mIM with not only higher $CO_2$ affinity but also higher intrinsic activity for catalytic $CO_2$RR.

## 4 Conclusion

In summary, a highly efficient NiNC catalyst (NiNC-2mIM) for $CO_2$RR is obtained by manipulating the nitrogen-containing

species via imidazole-based ZIF precursor-mediated regulation strategy. Pyrolysis of 2-methylimidazole Ni-ZIF induces the production of NiNC-2mIM with high content of pyridinic N species, which not only endows it with improved affinity for $CO_2$ but also engineers highly active pyridinic N-Ni sites to produce CO from $CO_2$RR, the $FE_{CO}$ reaches 98% at -1.0 V (vs. RHE) with a current density of 55 mA $cm^{-2}$, the catalytic performance for $CO_2$RR outperforms many previously reported Ni-based nanocatalysts. XRD and SEM reveal that pyrolysis of imidazole-based Ni-ZIF produces Ni nanocatalyst supported on N-doped carbon, XPS characterization demonstrates that the NiNC-2mIM catalyst derived from 2-methylimidazole Ni-ZIF possess higher content of pyridinic N and Ni-N motif with lower polarity as compared to the NiNC-IM and NiNC-2eIM catalysts. Underwater $CO_2$ bubble contact angle measurements manifest that the NiNC-2mIM catalyst possesses $CO_2$-philic surface, whereas the NiNC-IM and NiNC-2eIM exhibit lower affinity for $CO_2$. This difference is caused by the more abundant pyridinic N species in the NiNC-2mIM than in the NiNC-IM and NiNC-2eIM, which has been identified by $H_3PO_4$ treatment experiments. $H_3PO_4$ treatment protonates pyridinic N and weakens the electron donation from pyridinic N to $Ni^{2+}$, therefore, the electrochemical activity of the NiNC-2mIM undergoes a distinctly decrease. This work elucidates the critical role of engineering pyridinic N in N-doped carbon support for Ni nanocatalyst, and provides an effective strategy of developing high-activity electrocatalysts for $CO_2$RR.

## Data availability

All data needed to support the conclusions in the paper are presented in the manuscript and the Electronic Supplementary Material. Additional data related to this paper may be requested from the corresponding author upon request."

## Acknowledgements

This work was financially supported by National Natural Science Foundation of China (21671154 and U1732147), the Key Laboratory of Icing and Anti/De-icing of CARDC (No. IADL 20230106) and "the 14th Five Year Plan" Hubei Provincial advantaged characteristic disciplines (groups) project of Wuhan University of Science and Technology (2023A0501).

## Declaration of competing interest

All the contributing authors report no conflict of interests in this work.

## Author contribution statement

Xin Cui: Data curation (Lead), formal analysis (Lead), investigation (Lead), writing-original draft (Equal). Xiaona Meng: Data curation (Supporting), formal analysis (Supporting), investigation (Supporting), methodology (Supporting). Weixiong Huang: Data curation (Supporting), formal analysis (Supporting), methodology (Supporting). Bo Zhang: Data curation (Supporting), investigation (Supporting). Ping Chen: Data curation (Supporting), formal analysis (Supporting). Min Ruan: Methodology (Equal), project administration (Equal), resources (Equal), software (Lead), supervision (Equal). Lilin Lu: Conceptualization (Lead), funding acquisition (Lead), project administration (Equal), resources (Lead), supervision (Equal), writing-review & editing (Lead). All the authors have approved the final manuscript.

## Informed consent

Not applicable.

## Ethics statement

Not applicable.

## Use of AI statement

None.

## References

[1] Wu Q J, Si D H, Dong Y L, et al. Steering $CO_2$ electroreduction to hydrocarbons over 2D thiol-based conductive metal-organic framework[J]. Science Bulletin, 2025, 70(7): 1107-1117.

[2] Xie W, Li B, Liu L, et al. Advanced systems for enhanced $CO_2$ electroreduction[J]. Chemical Society Reviews, 2025,54, 898-959.

[3] Wang H, Shang B, Choi C, et al. Enhanced methanol production from photothermal $CO_2$ reduction via multilevel interface design[J]. Nano Research, 2025, 18(2): 94907160.

[4] Jin S, Hao Z, Zhang K, et al. Advances and challenges for the electrochemical reduction of $CO_2$ to CO: from fundamentals to industrialization[J]. Angewandte Chemie International Edition, 2021, 133(38): 20795-20816.

[5] Ma J, Yan J, Xu J, et al. Dynamic ion exchange engineering BiOI-derived $Bi_2O_2CO_3$ to promote $CO_2$ electroreduction for efficient formate production[J]. Chemical Engineering Journal, 2023, 455: 140926.

[6] He Y, Li Y, Zhang J, et al. Low-temperature strategy toward Ni-NC@ Ni core-shell nanostructure with Single-Ni sites for efficient $CO_2$ electroreduction[J]. Nano Energy, 2020, 77: 105010.

[7] Liang S, Huang L, Gao Y, et al. Electrochemical reduction of $CO_2$ to CO over transition metal/N-doped carbon catalysts: the active sites and reaction mechanism[J]. Advanced Science, 2021, 8(24): 2102886.

[8] Daiyan R, Chen R, Kumar P, et al. Tunable syngas production through $CO_2$ electroreduction on cobalt-carbon composite electrocatalyst[J]. ACS Applied Materials & Interfaces, 2020, 12(8): 9307-9315.

[9] Zhang W, Mehmood A, Ali G, et al. Nickel Nanocluster-Stabilized Unsaturated Ni-$N_3$ Atomic Sites for Efficient $CO_2$-to-CO Electrolysis at Industrial-Level Current[J]. Angewandte Chemie International Edition, 2025, 64(13): e202424552.

[10] Ren W, Tan X, Yang W, et al. Isolated diatomic Ni-Fe metal-nitrogen sites for synergistic electroreduction of $CO_2$[J]. Angewandte Chemie International Edition, 2019, 58(21): 6972-6976.

[11] Jia M, Choi C, Wu T S, et al. Carbon-supported Ni nanoparticles for efficient $CO_2$ electroreduction[J]. Chemical Science, 2018, 9(47): 8775-8780.

[12] Lu Q, Jiao F. Electrochemical $CO_2$ reduction: Electrocatalyst, reaction mechanism, and process engineering[J]. Nano Energy, 2016, 29: 439-456.

[13] Ju W, Bagger A, Hao G P, et al. Understanding activity and selectivity of metal-nitrogen-doped carbon catalysts for electrochemical reduction of $CO_2$[J]. Nature Communications, 2017, 8(1): 1-9.

[14] Guo M, Du S, Yang G, et al. MOF-derived N-doped carbon-wrapped Ni electrocatalyst for highly efficient electrochemical $CO_2$ reduction to CO[J]. Energy & Fuels, 2024, 38(12): 11043-11050.

[15] Zhang L, Feng J, Liu S, et al. Atomically dispersed Ni-Cu catalysts for pH-universal $CO_2$ electroreduction[J]. Advanced materials, 2023, 35(13): 2209590.

[16] Chen Y, Zhang J, Yang L, et al. Recent advances in non-precious metal-nitrogen-carbon single-site catalysts for $CO_2$ electroreduction reaction to CO[J]. Electrochemical Energy Reviews, 2022, 5(4): 11.

[17] Pan Q, Chen Y, Jiang S, et al. Insight into the active sites of M-N-C single-atom catalysts for electrochemical $CO_2$ reduction[J]. EnergyChem, 2023, 5(6): 100114.

[18] Pang Q, Fan X, Sun K, et al. Nickel-Nitrogen-Carbon (Ni-N-C) Electrocatalysts Toward $CO_2$ electroreduction to CO: Advances, Optimizations, Challenges, and Prospects[J]. Energy & Environmental Materials, 2024, 7(5): e12731.

[19] Liao Q, Song Y, Li W, et al. Perspectives of nickel-based catalysts in carbon dioxide electroreduction[J]. Journal of Materials Science & Technology, 2025, 218: 108-125.

[20] Sun Y, Liu F, Wang X, et al. Highly selective $CO_2$ electroreduction to CO by the synergy between Ni-N-C and encapsulated Ni

nanoparticles[J]. Dalton Transactions, 2023, 52(4): 928-935.
[21] Tan D, Cui C, Shi J, et al. Nitrogen-carbon layer coated nickel nanoparticles for efficient electrocatalytic reduction of carbon dioxide[J]. Nano Research, 2019, 12(5): 1167-1172.
[22] Liu S, Yang H, Huang X, et al. Identifying active sites of nitrogen-doped carbon materials for the $CO_2$ reduction reaction[J]. Advanced Functional Materials, 2018, 28(21): 1800499.
[23] Pan F, Zhang H, Liu Z, et al. Atomic-level active sites of efficient imidazolate framework-derived nickel catalysts for $CO_2$ reduction[J]. Journal of Materials Chemistry A, 2019, 7(46): 26231-26237.
[24] Han X, Zhang T, Biset-Peiró M, et al. Engineering the interfacial microenvironment via surface hydroxylation to realize the global optimization of electrochemical $CO_2$ reduction[J]. ACS Applied Materials & Interfaces, 2022, 14(28): 32157-32165.
[25] Cheng Y, Li Q, Salaman M I B, et al. Microenvironment Tailoring for Electrocatalytic CO2 Reduction: Effects of Interfacial Structure on Controlling Activity and Selectivity[J]. Journal of the American Chemical Society, 2025, 147(15): 12438-12448.
[26] Shibuya R, Takeyasu K, Guo D, et al. Chemisorption of $CO_2$ on Nitrogen-Doped Graphitic Carbons[J]. Langmuir, 2022, 38(47): 14430-14438.
[27] Li Y, Adli N M, Shan W, et al. Atomically dispersed single Ni site catalysts for high-efficiency $CO_2$ electroreduction at industrial-level current densities[J]. Energy & Environmental Science, 2022, 15(5): 2108-2119.
[28] Ismail F, Abdellah A, Lee H J, et al. Impact of nickel content on the structure and electrochemical $CO_2$ reduction performance of nickel-nitrogen-carbon catalysts derived from zeolitic imidazolate frameworks[J]. ACS Applied Energy Materials, 2022, 5(1): 430-439.
[29] Zhang Q, Huang Y, Cao R. Imidazolium-based materials for $CO_2$ electroreduction[J]. Acta Physico-Chimica Sinica, 2024, 40(4): 2306040.
[30] Jing Z Y, Si D H, Guo H, et al. Boosting $CO_2$ Electroreduction by Preactivation Strategy over Carbene-Based Metal-Organic Framework[J]. CCS Chemistry, 2024, 6(12): 3053-3064.
[31] Jiao L, Zhu J, Zhang Y, et al. Non-bonding interaction of neighboring Fe and Ni single-atom pairs on MOF-derived N-doped carbon for enhanced $CO_2$ electroreduction[J]. Journal of the American Chemical Society, 2021, 143(46): 19417-19424.
[32] Koshy D M, Chen S, Lee D U, et al. Understanding the origin of highly selective $CO_2$ electroreduction to CO on Ni, N-doped carbon catalysts[J]. Angewandte Chemie International Edition, 2020, 59(10): 4043-4050.
[33] Liang S, Jiang Q, Wang Q, et al. Revealing the real role of nickel decorated nitrogen-doped carbon catalysts for electrochemical reduction of $CO_2$ to CO[J]. Advanced Energy Materials, 2021, 11(36): 2101477.
[34] Niu Y, Zhang C, Wang Y, et al. Confining Chainmail-Bearing Ni Nanoparticles in N-doped Carbon Nanotubes for Robust and Efficient Electroreduction of $CO_2$[J]. ChemSusChem, 2021, 14(4): 1140-1154.
[35] Wen C F, Mao F, Liu Y, et al. Nitrogen-stabilized low-valent Ni motifs for efficient $CO_2$ electrocatalysis[J]. ACS Catalysis, 2019, 10(2): 1086-1093.
[36] Yang X, Si D H, Li H F, et al. Robust imidazole-linked Ni-phthalocyanine-based covalent-organic framework for $CO_2$ electroreduction in the full pH range[J]. Materials Chemistry Frontiers, 2024, 8(6): 1611-1618.
[37] Zhang M D, Huang J R, Shi W, et al. Self-Accelerating Effect in a Covalent-Organic Framework with Imidazole Groups Boosts Electroreduction of $CO_2$ to CO[J]. Angewandte Chemie International Edition, 2023, 135(42): e202308195.
[38] Rong X, Wang H J, Lu X L, et al. Controlled synthesis of a vacancy-defect single-atom catalyst for boosting $CO_2$ electroreduction[J]. Angewandte Chemie International Edition, 2020, 132(5): 1977-1981.
[39] M.D. Segall, J.D.L. Philip, M.J. Probert, C.J. Pickard, P.J. Hasnip, S.J. Clark, M.C. Payne, First-principles simulation: ideas, illustrations and the CASTEP code, J. Phys.: Condens. Matter, 14 (2002) 2717.
[40] E. M, Generalized Gradient Approximation Made Simple, Phys. Rev.Lett., 77 (1996) 3865.
[41] D. Vanderbilt, Soft self-consistent pseudopotentials in a generalized eigenvalue formalism, Physical Review B, 41 (1990) 7892-7895.
[42] B.G. Pfrommer, M. Côté, S.G. Louie, M.L. Cohen, Relaxation of Crystals with the Quasi-Newton Method, Journal of Computational Physics, 131 (1997) 233-240.
[43] N. Govind, M. Petersen, G. Fitzgerald, D. King-Smith, J. Andzelm, A generalized synchronous transit method for transition state location, Comp.Mater. Sci., 28 (2003) 250-258.
[44] Liu Z, Li G, Alalouni M R, et al. Facile preparation of a Ni-imidazole compound with high activity for ethylene dimerization[J]. Chemical Communications, 2024, 60(2): 188-191.
[45] Zhu Z, Li Z, Wei X, et al. Achieving efficient electroreduction of $CO_2$ to CO in a wide potential window by encapsulating Ni nanoparticles in N-doped carbon nanotubes[J]. Carbon, 2021, 185: 9-16.
[46] Jia C, Tan X, Zhao Y, et al. Sulfur-dopant-promoted electroreduction of $CO_2$ over coordinatively unsaturated Ni-$N_2$ moieties[J]. Angewandte Chemie International Edition, 2021, 60(43): 23342-23348.
[47] Wang Q, Liu K, Hu K, et al. Attenuating metal-substrate conjugation in atomically dispersed nickel catalysts for electroreduction of $CO_2$ to CO[J]. Nature Communications, 2022, 13(1): 6082.
[48] Yang H, Lin Q, Zhang C, et al. Carbon dioxide electroreduction on single-atom nickel decorated carbon membranes with industry compatible current densities[J]. Nature Communications, 2020, 11(1): 593.
[49] Lu Q, Chen C, Di Q, et al. Dual role of pyridinic-N doping in carbon-coated Ni nanoparticles for highly efficient electrochemical $CO_2$ reduction to CO over a wide potential range[J]. ACS Catalysis, 2022, 12(2): 1364-1374.
[50] Yan J, Ma H, Ni J, et al. Engineering iron carbide catalyst with aerophilic and electron-rich surface for improved electrochemical $CO_2$ reduction[J]. Journal of Colloid and Interface Science, 2023, 648: 558-566.
[51] Cho J H, Lee C, Hong S H, et al. Transition metal ion doping on ZIF-8 enhances the electrochemical $CO_2$ reduction reaction[J]. Advanced Materials, 2023, 35(43): 2208224.

# Electronic Supplementary Material

# $CO_2$-philic NiNC nanocatalyst regulation mediated by imidazole-based ZIF for high-efficiency $CO_2$ electroreduction

Xin Cui,[1,2] Xiaona Meng,[1,2] Weixiong Huang,[1,2] Bo Zhang,[1,2] Ping Chen,[1,2] Min Ruan, [3] ✉, and Lilin Lu [1,2] ✉

[1] *The State Key Laboratory of Refractories and Metallurgy, Wuhan University of Science and Technology, Wuhan 430081, China*
[2] *Hubei Province Key Laboratory of Coal Conversion and New Carbon Materials, Wuhan University of Science and Technology, Wuhan 430081, China*
[3] *Hubei Key Laboratory of Mine Environmental Pollution Control & Remediation, Mineral Processing Research Institute, Hubei Polytechnic University, Huangshi 435003, China*

Supporting information to https://doi.org/10.26599/NR.2026.94908559

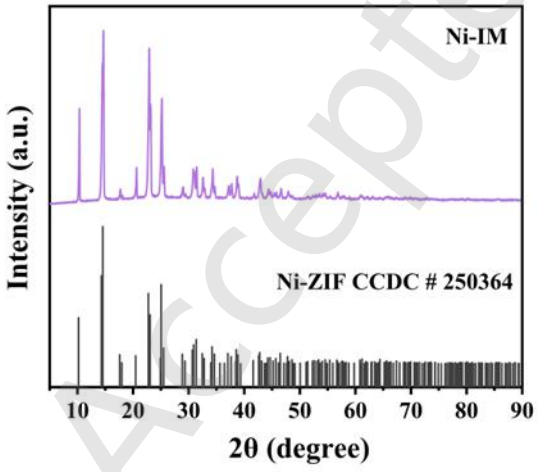


**Figure S1** XRD pattern of Ni-IM.



Address correspondence to Lilin Lu, lulilin@wust.edu.cn; Min Ruan, ruanmin@hbpu.edu.cn

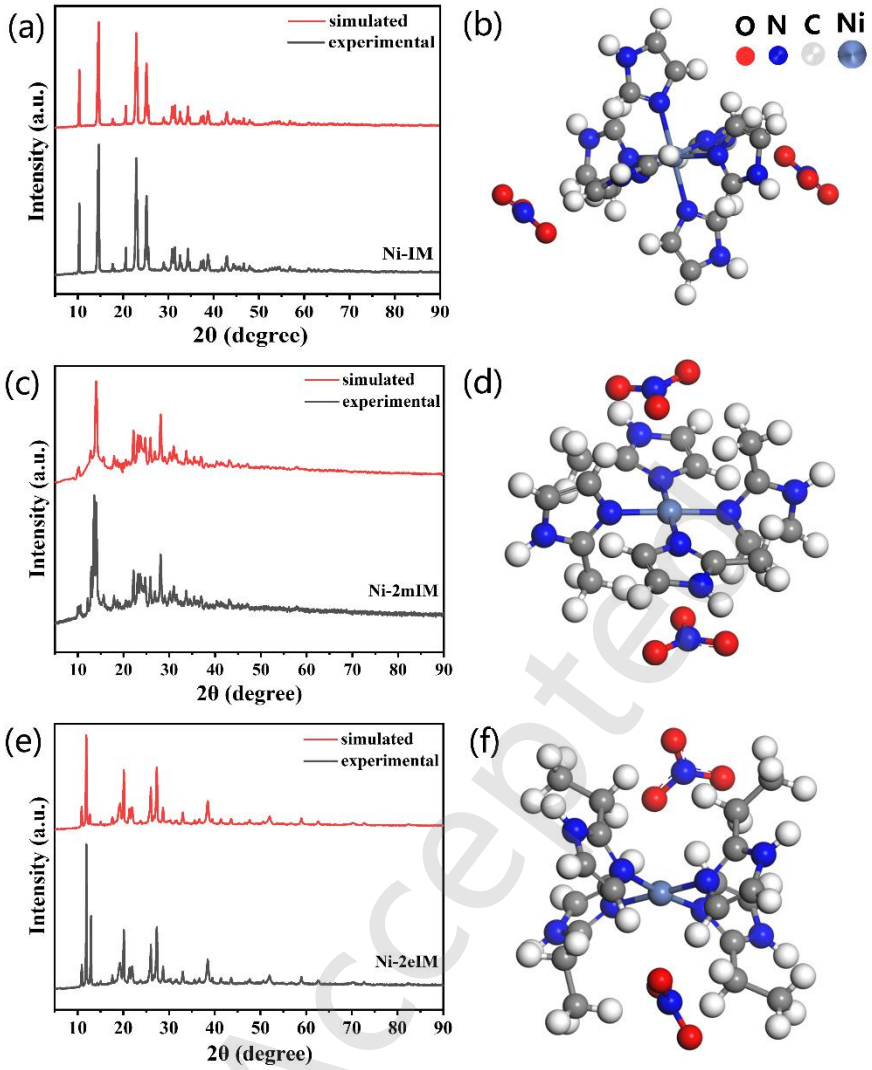


**Figure S 2** The simulated XRD patterns and structural models of (a,b) Ni-IM, (c, d) Ni-2mIM and (e, f) Ni-2eIM.

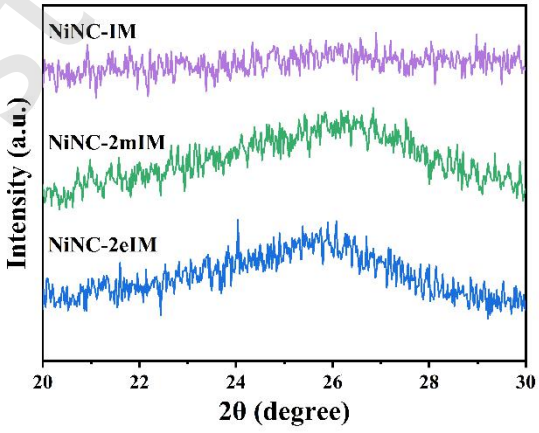


**Figure S 3** Magnified XRD patterns of NiNC-IM, NiNC-2mIM and NiNC-2eIM catalysts in the range of 20°-30°.

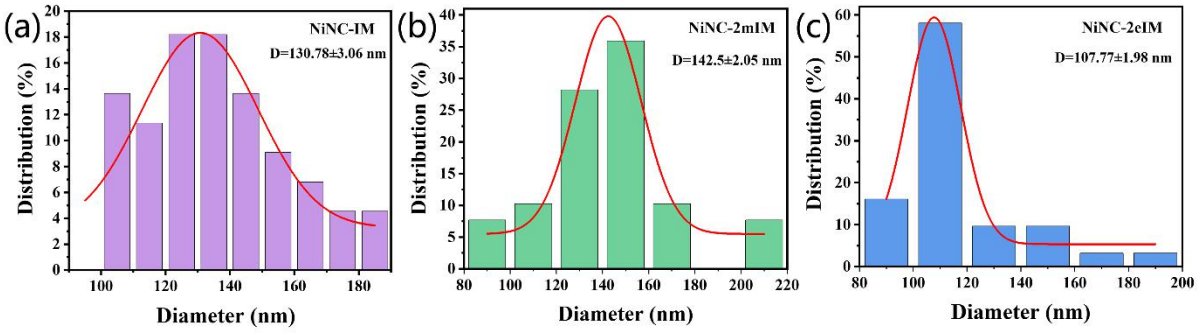


**Figure S 4** Ni particle size statistics in (a) NiNC-IM, (b) NiNC-2mIM and (c) NiNC-2eIM.

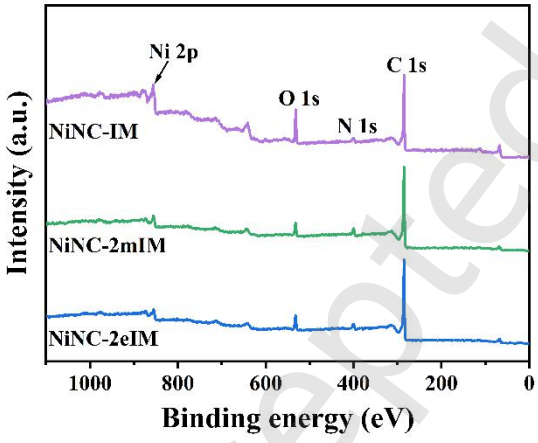


**Figure S 5** Overall survey spectra of NiNC-IM, NiNC-2mIM and NiNC-2eIM.

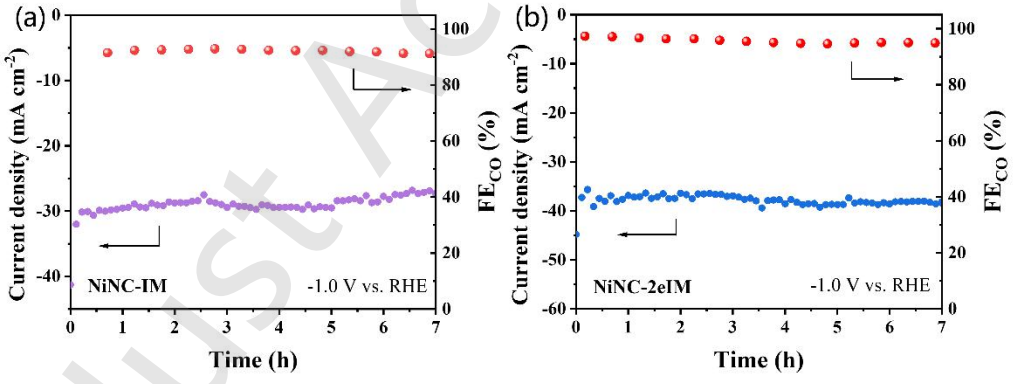


**Figure S 6** Durability testing of a) NiNC-IM and b) NiNC-2eIM at -1.0 V (vs. RHE).

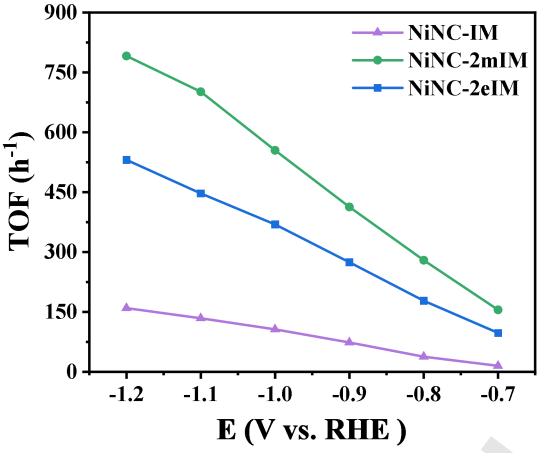


**Figure S 7** TOF of $CO_2$RR catalyzed by NiNC-IM, NiNC-2mIM, and NiNC-2eIM.

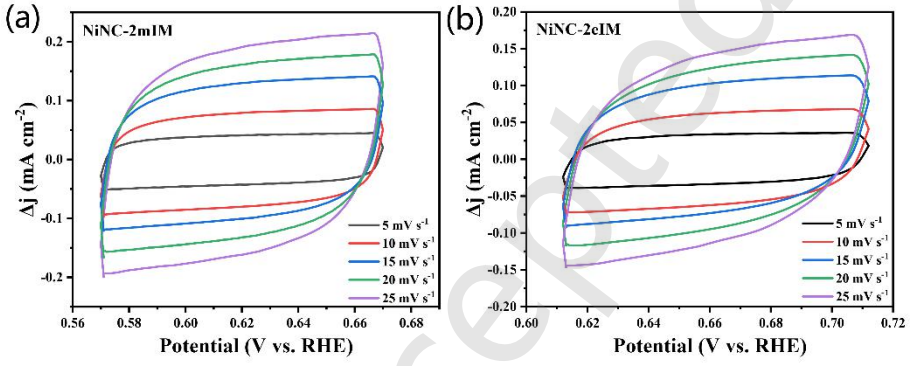


**Figure S 8** CV curves at the scan rates from 5 mV $s^{-1}$ to 25 mV $s^{-1}$ of (a) NiNC-2mIM and (b) NiNC-2eIM.

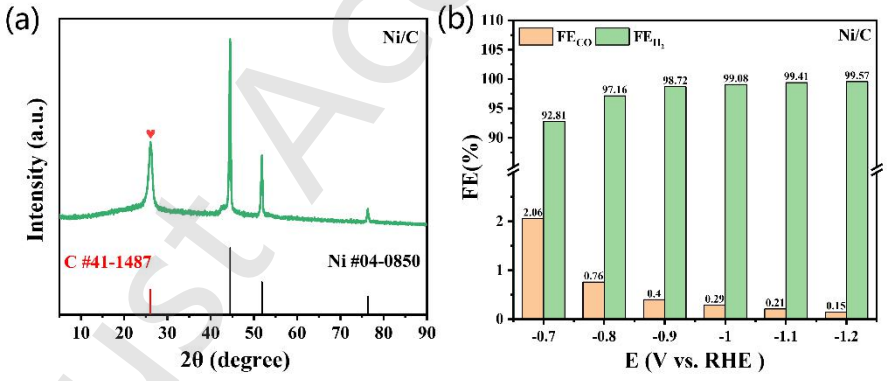


**Figure S 9** (a) XRD pattern and (b) electrochemical performance of Ni/C in H-type cell. The Ni/C catalyst was prepared by pyrolysis of the mixture of nickel nitrate and glucose at 800℃ in an Ar atmosphere.

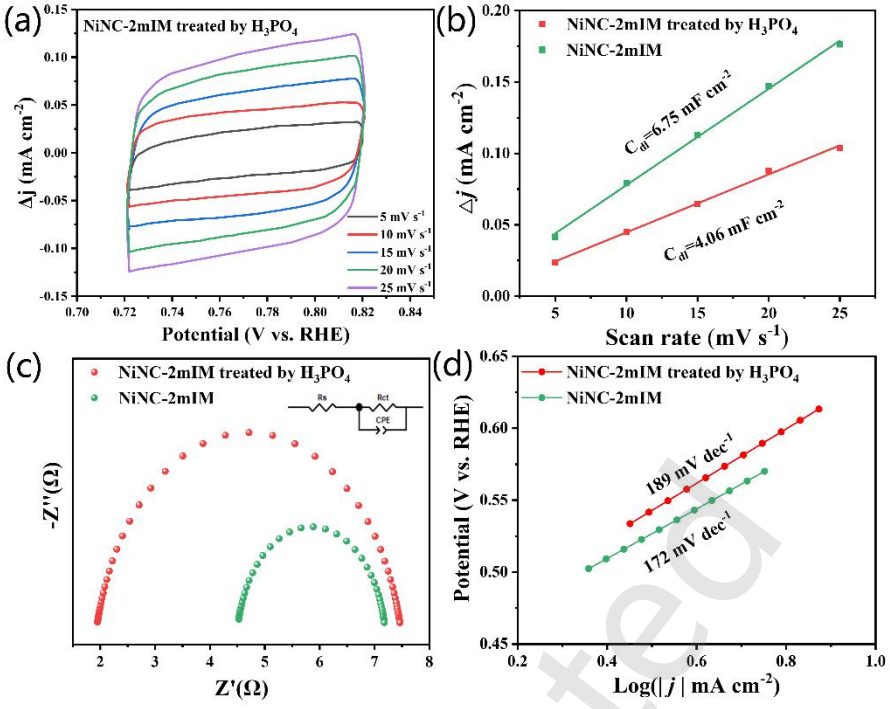


**Figure S 10** (a) CV curves at the scan rates from 5 mV $s^{-1}$ to 25 mV $s^{-1}$, (b) electrochemical $C_{dl}$, (c) EIS spectra and (d) Tafel plots of $H_3PO_4$ treated NiNC-2mIM. Electrochemical $C_{dl}$, EIS spectra and Tafel plots of of the fresh NiNC-2mIM are displayed for comparison.